Research Square

Preprints are preliminary reports that have not undergone peer review.
They should not be considered conclusive, used to inform clinical practice,
or referenced by the media as validated information.

Drought to Flood Abrupt Alternation Events Across Monsoon Region in China: Characteristics, Mechanisms, and Crop Exposure

Jun Liu
China Meteorological Administration
Yingxiao Sun
NUIST: Nanjing University of Information Science and Technology
Chunxuan Zhao
NUIST: Nanjing University of Information Science and Technology
Tong Jin
Digital Theatre Ltd
Xuehua An
NUIST: Nanjing University of Information Science and Technology
Jiayi Mu
NUIST: Nanjing University of Information Science and Technology
Qianrong ma
maqianron_g@163.com
NUIST: Nanjing University of Information Science and Technology https://orcid.org/0000-0001-7789-5293
Shanlei Sun
NUIST: Nanjing University of Information Science and Technology
Hao Wu
China Meteorological Administration

Research Article

Keywords: drought to flood abrupt alternation events, monsoon region of China, jet-waveguide interaction, potential vorticity gradient, crop exposure

Posted Date: November 4th, 2026

DOI: https://doi.org/10.21203/rs.3.rs-10952103/v1

License: This work is licensed under a Creative Commons Attribution 4.0 International License.
Read Full License

Abstract

Climate change is altering the frequency and intensity of hydroclimatic extremes, increasing the likelihood of drought to flood abrupt alternation (DTFAA) events which creates compound risks. Here, we identify DTFAA events across the monsoon region of China (MRC) during May–September from 1961 to 2023 using the daily Standardized Weighted Average Precipitation index. We identify 3,575 DTFAA events, with most transitions occurring within 1–2 days and a modest maximum in June. Generally, DTFAA frequency and intensity in MRC increase significantly at rates of 0.29 times decade^{-1} and 0.26 decade^{-1}, respectively, with high frequencies concentrated in the middle and lower Yangtze River Basin, southern coastal China, and parts of North and Southwest China. Dynamically, governed by jet-waveguide interaction, the transition initiates with high-latitude easterly anomalies anchoring upstream blocking and the westward-extending subtropic high priming baroclinicity. Subsequently, the intensified and westward-extending subtropical jet establishes a mid-latitude meridional potential vorticity gradient conduit, routing trapped energy in blocking downstream to drive deep dynamic suction and moisture convergence, unleashing the abrupt flooding. Furthermore, crop exposure is crop-specific heterogeneous: maize and wheat show extensive high-exposure belts, whereas rice exposure is more fragmented; maize exhibits significant increases in both frequency and intensity exposure during 2000–2019. These results demonstrate that DTFAA events in the MRC arise from coordinated large-scale circulation and moisture-transport processes and that their agricultural consequences are strongly crop and region dependent, providing a dynamical and impact-oriented framework for improving monitoring, prediction, and adaptation to rapid hydroclimatic transitions.

1. Introduction

By accelerating and reorganizing the global hydrological cycle, climate change is altering the frequency, intensity, and temporal sequencing of hydroclimatic extremes, increasing the exposure of human societies and natural ecosystems to multi-hazard risks (IPCC, 2023; Seneviratne et al., 2021; Wasko, 2022). Although considerable attention has been devoted to isolated droughts and floods, rapid transitions between these contrasting hydroclimatic states represent a distinct class of compound extreme event. Specifically, drought to flood abrupt alternation events (DTFAA), marked by swift shifts from severe dryness to wet extremes, challenge conventional hazard paradigms (Shi et al., 2021). Because these events occur sequentially rather than independently, their compounded effects trigger acute, cascading impacts: antecedent drought degrades vegetation, alters soil structure, and diminishes infiltration capacity, thereby amplifying surface runoff and exacerbating subsequent flooding (Wang et al., 2023; Wu et al., 2026). Moreover, both the frequency and intensity of DTFAA events have increased significantly at the global scale since 2000 (Barendrecht et al., 2024; Chen et al., 2025; Zhao et al., 2026). DTFAA events therefore pose challenges that differ fundamentally from those associated with isolated droughts or floods, with important implications for water resources, ecosystem functioning, agricultural production, and disaster risk management (Bai et al. 2023; Shi et al. 2024).

The monsoon region of China (MRC) is particularly vulnerable to rapid hydroclimatic shifts. Under continued climate change, DTFAA events in this region have increased markedly in both frequency and intensity (Wang et al. 2026a, b). Occurring predominantly during the main summer flood season, these events can trigger widespread basin-scale flooding, urban waterlogging, and substantial agricultural losses (Dai et al. 2026; Zhao et al. 2026). This hazard potential is exacerbated by the region's dense population, intensive agriculture, rapid urbanization, and escalating water demand, which collectively heighten regional exposure and socioeconomic vulnerability (Gu et al. 2026; Zhu et al. 2026). Recent events illustrate their destructive capacity. In 2011, prolonged winter–spring drought across the middle and lower reaches of the Yangtze River Basin was abruptly superseded by persistent torrential summer rains, resulting in over 1.34 billion yuan in direct economic losses, affecting more than 2 million residents, and inundating roughly 15,000 km² of farmland in Anhui Province alone (Yang et al., 2013). Similarly, during June–July 2023, North China experienced below-normal precipitation and widespread drought conditions, which were abruptly followed by extreme rainstorms across much of the region in early August. In Beijing alone, the event affected approximately 1.29 million people, caused 33 fatalities, and damaged approximately 15,000 ha of cropland (Chen et al. 2024). These representative cases demonstrate the substantial societal, economic, and agricultural consequences of DTFAA events and underscore the growing importance of understanding their characteristics and underlying physical mechanisms.

The increasing occurrence of DTFAA events is closely associated with intensification and reorganization of the hydrological cycle under global warming. Enhanced atmospheric moisture-holding capacity can intensify extreme precipitation, while increasing evaporative demand can accelerate surface drying, together increasing the likelihood of rapid transitions between anomalously dry and wet conditions (Gimeno et al., 2026; Na and Najafi, 2024; Roderick et al., 2019). These thermodynamic changes can amplify hydroclimatic contrasts and increase the risks associated with successive dry and wet extremes (Swain et al. 2025; Yin et al. 2023). However, thermodynamic forcing alone cannot fully explain the pronounced spatiotemporal heterogeneity of DTFAA events. Dynamic processes and land–atmosphere feedback can further regulate regional water imbalances, thereby modulating the occurrence, timing, and severity of rapid hydroclimatic transitions (Hu et al. 2025; Zhao et al. 2026). For example, He et al. (2025) reported an increase in DTFAA events during 1979–2022 that was primarily associated with enhanced variability in atmospheric moisture transport. Large-scale climate variability, particularly the El Niño–Southern Oscillation (ENSO), can also modulate these rapid transitions, with La Niña conditions potentially increasing their spatial extent and intensity. The dominant controls on DTFAA events further vary across climatic regions: vapor pressure deficit exhibits bidirectional relationships with DTFAA occurrence in tropical regions, whereas net radiation exerts bidirectional effects in arid regions (Wu et al., 2026). Beyond these large-scale thermodynamic and circulation-related controls, synoptic-scale atmospheric processes may play a critical role in triggering and sustaining rapid drought-to-flood transitions. Large-scale circulation anomalies can interact with blocking events, atmospheric rivers, jet-stream variability, and Rossby wave activity to alter moisture transport, precipitation persistence, and atmospheric stability, thereby facilitating abrupt transitions between anomalously dry and wet conditions

(De Vries et al. 2024; Henny and Kim 2025; Zhou et al. 2025; Zhao et al. 2026). Anthropogenic forcing may further influence the frequency and intensity of DTFAA events through its effects on radiative forcing, the hydrological cycle, and atmospheric circulation patterns (Gotte and Brunner 2024; Matanó et al. 2022; Seneviratne et al. 2021). Collectively, these findings indicate that DTFAA events emerge from interactions among processes operating across multiple spatial and temporal scales. Nevertheless, the relative importance of the mechanisms underlying the rapid evolution of events remain insufficiently understood.

Numerous studies have investigated the characteristics and mechanisms of DTFAA events in the MRC, primarily at monthly or seasonal timescales (Wu et al., 2006; Shan et al., 2018; Yang et al., 2022; Ji et al., 2025). However, the temporal resolution of these approaches may be insufficient to capture the rapid evolution of individual drought-to-flood transitions. Wang et al. (2021) emphasized that DTFAA events can involve an abrupt transition from a persistent drought period lasting approximately 10–20 days to a period of intense precipitation. Such rapid transitions highlight the need for analyses at daily timescales to better characterize event evolution and identify the dynamic processes governing their development. Moreover, although previous studies have examined the climatic characteristics and physical drivers of DTFAA events, comparatively less attention has been paid to the extent to which their underlying mechanisms vary across climate regimes and how these hazards translate into agricultural risks.

To address these gaps, this study investigates the characteristics and mechanisms of DTFAA events across MRC using a daily-scale index designed to capture rapid hydroclimatic transitions. We further examine the key dynamic processes governing the evolution of DTFAA events. In addition, we assess the vulnerability of agricultural land to DTFAA events to evaluate how climate-regime-dependent hazards translate into spatially heterogeneous agricultural risks. The results are expected to improve understanding of rapid hydroclimatic transitions in the MRC and provide a scientific basis for strengthening agricultural risk assessment and adaptation to compound hydroclimatic extremes. The remainder of this paper is organized as follows. Section 2 describes the data and methods used in this study. Section 3 presents the spatiotemporal characteristics of DTFAA events and investigates their associated multiscale dynamic mechanisms and agricultural risks. Section 4 summarizes the main findings and discusses their broader implications.

2. Data and Methods

2.1 Datasets

Daily precipitation observations for 1961–2023 were obtained from the National Meteorological Information Center of the China Meteorological Administration (CMA). After quality control procedures and homogeneity assessments 1,903 meteorological stations were selected across the MRC (Zhang et al. 2025). To investigate the atmospheric processes associated with DTFAA events, we used daily fields from the fifth-generation European Centre for Medium-Range Weather Forecasts (ECMWF) Reanalysis v5 datasets (ERA5, Hersbach et al. 2020). The variables analyzed include geopotential height, zonal wind,

meridional wind, and vertically integrated water vapor transport (IVT). The atmospheric circulation fields were analyzed on a horizontal grid of 1.0° × 1.0° and at 12 vertical levels. Crop phenological information was obtained from the ChinaCropPhen1km dataset, which provides annual crop phenology data at a spatial resolution of 1 km for the period 2000–2019 (Luo et al. 2020). The dataset includes phenological information for the three major cereal crops—wheat, maize, and rice—across China. These data were used to characterize the temporal overlap between DTFAA occurrence and crop growing periods and to support the assessment of agricultural exposure and risk.

2.2 Identification DTFAA events

This study investigates DTFAA events across the MRC during the flood season (May–September) for 1961–2023. This period accounts for approximately 60%–70% of the annual total and coincides with the most active period of regional hydrological cycling and hydroclimatic extremes (Zhai et al. 2005). DTFAA events were identified using the Standardized Weighted Average Precipitation (SWAP) index provided by Lu (2009). The SWAP index is derived from weighted average precipitation and subsequently standardized using a Gamma distribution, enabling the identification of anomalously dry and wet conditions at the daily timescale.. Following Zhao et al. (2026), drought and flood events were defined as periods during which the SWAP index remained below − 1 and above 1, respectively, for at least 10 consecutive days. The 10 days threshold conforms to the National Standard of China for Meteorological Drought Classification (GB/T 20481–2006) and effectively filters out transient daily precipitation noise from sustained hydroclimatic extremes.

The identification of DTFAA events additionally requires a physically meaningful definition of the transition period between drought and flood conditions. A drought event rarely transition directly into a flood event immediately after the cessation of drought, because drought recovery involves sustained precipitation and progressive adjustment of soil moisture and hydrological conditions. Drought accordingly termination occurs after drought-related indices return to non-drought conditions and remain so for approximately 7 consecutive days (He et al. 2015). We therefore set an 8-day interval as the maximum transition period between the termination of a drought and the onset of a subsequent flood. This interval is intended to account for the recovery from drought and the associated hydrological adjustment while preserving the rapid nature of the drought-to-flood transition. Accordingly, sequential drought and flood events were classified as a DTFAA event. This threshold is consistent with previous investigations of rapid drought-to-flood transitions in the MRC (Ji et al. 2025; Zhao et al. 2026). In addition, sensitivity tests using alternative transition periods demonstrate that the key characteristics of DTFAA events are insensitive to the threshold choice, supporting the robustness of the 8-day criterion (Fig.. S1). A total of 3,575 DTFAA events were identified, and Fig. 1 exhibits a DTFAA event evolution at Lingbi Station.

2.3 Meridional potential vorticity gradient

The non-dimensional equivalent barotropic meridional potential vorticity gradient (PV_y) at 200 hPa is calculated to diagnose the waveguide evolution and wave breaking associated with DTFAA events (Luo

et al., 2019):

$$\mathrm{PV}_y = \beta - U_{yy} + FU$$

1

where U is 200-hPa zonal wind, and $U_{yy} = \partial^2 U / \partial y^2$. The non-dimensional planetary vorticity gradient is defined as $\beta = \beta_0 L'^2 / U'$, where β_0 is the meridional gradient of the Coriolis parameter at a reference latitude ϕ_0, and $L' \approx 1.0 \times 10^6 \mathrm{m}$ is the characteristic horizontal length scale. The parameter $F = \left(L' / R_d \right)^2$ denotes the non-dimensional barotropic stratification parameter, where R_d is the Rossby radius of deformation. Since $R_d \approx L' \approx 1000 \backslash : \mathrm{km}$, we adopt $F \approx 1.0$. The PV_y acts as a dynamic metric governing Rossby wave propagation and large-scale circulation persistence. A reduced or negative background PV_y favors the maintenance of blocking systems and persistent ridge anomalies by suppressing downstream wave energy dispersion and enhancing local nonlinearity. Conversely, a stronger background PV_y favors downstream wave energy dispersion and waveguide propagation.

2.4 Calculation of crop exposure to DTFAA events

To quantify the potential exposure of agricultural systems to drought-to-flood abrupt alternation (DTFAA) events, we assessed the exposure of three major staple crops—wheat, maize, and rice, to DTFAA hazards. The exposure assessment followed the hazard–exposure framework of Li et al. (2025), in which exposure is quantified by integrating the frequency of hazardous events with the amount of exposed elements within the corresponding affected area. The agricultural exposure to DTFAA events was calculated as:

$$\mathrm{Exposure}_{crop} = \sum_{i=1}^{n} crop\left(x\right)_i \times \mathrm{DTFAA}_s$$

2

where DTFAA_s is the frequency of DTFAA in station i. And the $crop\left(x\right)_i$ represents the different crop (x) areas affected by station i. The spatial area represented by each meteorological station was delineated using the Thiessen polygon method. Specifically, each station was assigned a Thiessen polygon, within which all locations were assumed to be represented by the DTFAA characteristics observed at that station. Crop exposure was then quantified by combining the DTFAA frequency at each station with the corresponding area of each crop contained within its Thiessen polygon.

3. Results

3.1 Spatiotemporal characteristics of DTFAA events in MRC

Figure 2 shows the spatial distributions of DTFAA mean frequency and intensity across the MRC during 1961–2023. DTFAA frequency exhibits pronounced spatial heterogeneity, with relatively high values occurring primarily in the middle and lower reaches of the Yangtze River Basin, North China, and parts of Southwest China, whereas lower frequencies are generally observed toward the northwestern margins of the study region (Fig. 2a). Frequencies exceeding 1.2 events per decade are mainly concentrated in the middle and lower reaches of the Yangtze River Basin and the southern coastal region, while frequencies below 0.4 events per decade occur predominantly along the northwestern fringe. The spatial distribution of DTFAA intensity exhibits a pattern that is broadly consistent with, but not identical to, that of event frequency. The most severe events, cluster predominantly over North China and the Pearl River Delta, whereas weaker events dominate the northwestern MRC. (Fig. 2b). The partial spatial correspondence between frequency and intensity suggests that regions experiencing frequent DTFAA events do not necessarily experience the most intense events.

Transition duration is strongly concentrated within 1–2 days, indicating that most events involve an exceptionally rapid shift from drought to flood conditions. The monthly distribution of DTFAA occurrence shows a modest maximum in June, although events occur throughout the May–September flood season and differences among months are relatively small. The seasonal concentration of events is broadly consistent with the active period of the East Asian summer monsoon, suggesting an important role of seasonal monsoon evolution in modulating the occurrence of rapid hydroclimatic transitions. Overall, DTFAA events are spatially heterogeneous across the MRC, with frequent and intense events concentrated primarily in the humid southeastern monsoon region and parts of North China.

Figure 3 further illustrates the spatiotemporal changes of DTFAA frequency and intensity across the MRC during 1961–2023. Spatially, the trends exhibit substantial regional heterogeneity. Positive trends dominate the southern and eastern portions of the MRC, whereas weak negative or near-zero trends occur mainly along the western and northern margins. Statistically significant positive trends are primarily concentrated in the lower reaches of the Yangtze River Basin and the southeastern coastal region, indicating that these areas have experienced robust increases in DTFAA occurrence and intensity over the past six decades. The inset distributions further quantify the spatial prevalence of these trends. Approximately 56.5% of stations exhibit increasing trends in DTFAA frequency, although only about 3% show statistically significant increases (Fig. 3a). The statistically significant frequency trends are concentrated primarily in North China and the lower Yangtze River Basin. Similarly, approximately 56.9% of stations exhibit increasing trends in DTFAA intensity (Fig. 3b), while statistically significant trends occur only over a limited portion of the study region.

Despite the substantial spatial heterogeneity, the regional mean time series reveal significant increasing trends in both DTFAA events frequency and intensity. The frequency and intensity increase at rates of 0.29 times per decade and 0.26 per decade ($p < 0.05$), respectively. The marked difference in trend

magnitudes suggests that the observed elevation in DTFAA risk over the MRC is driven primarily by a higher frequency of transition events, rather than by a systematic amplification of intensity. Large-scale circulation adjustments, such as enhanced intraseasonal variability of the monsoon, can respond rapidly and thus preferentially drive the increase in event frequency (Liu et al., 2026). In contrast, event severity is further moderated by local land-surface conditions (e.g., soil moisture and vegetation), which evolve on much slower timescales and therefore contribute less to the observed intensification trend over the study period (Song et al., 2026). Notably, average DTFAA events exceeded 4 times in 2020, the highest value on record. The pronounced spatial heterogeneity and the stronger increase in event frequency relative to intensity motivate further investigation into the multiscale atmospheric processes responsible for the occurrence and intensification of DTFAA events.

3.2 Evolution of atmospheric circulation anomalies during DTFAA events

To identify robust large-scale features, regional DTFAA events were identified using a minimum threshold of six co-occurring stations, yielding 71 qualifying events for composite analysis. The resulting composite evolution of the 200-hPa circulation provides compelling evidence of a pronounced reorganization of the upper-tropospheric circulation preceding and accompanying DTFAA events over the MRC (Fig. 4). From Day − 8 to Day − 6, the circulation is characterized by alternating positive and negative U200 anomalies across the mid–high latitudes of Eurasia, indicating substantial modulation of the background westerly flow. During this early stage, enhanced westerlies are evident over the region west of the MRC, while negative U200 anomalies emerge farther downstream. At the same time, the 200-hPa westerly jet remains broadly zonally oriented across the subtropical–midlatitude region, and the South Asian High (SAH), represented by the 12,500-gpm contour, remains located predominantly to the south of the MRC (Figs. 4a, 4b). These features indicate that the upper-level circulation has already begun to depart from its climatological configuration several days before the drought-to-flood transition. From Day − 6 to Day − 4, the longitudinal contrast in U200 anomalies becomes more coherent. Positive U200 anomalies strengthen over central Asia, whereas negative anomalies become increasingly evident downstream toward East Asia. This eastward progression of the zonal-wind anomaly pattern suggests a gradual redistribution of upper-tropospheric westerly momentum along the Eurasian midlatitude flow. Meanwhile, the anomalous wind vectors indicate an organized circulation perturbation extending from western and central Asia toward East Asia (Fig. 4c). The circulation change becomes substantially stronger during Day − 2 to Day 0. By Day − 2, a pronounced dipole-like structure is evident, with positive U200 anomalies over central Asia and strong negative anomalies emerging over northeastern East Asia (Fig. 4d). At Day 0, the negative U200 anomalies intensify markedly over eastern China and adjacent regions, accompanied by significant anomalous winds. This evolution indicates a rapid weakening and reorganization of the upper-level westerly flow over the MRC near the onset of the DTFAA event (Fig. 4e). Simultaneously, the 200-hPa westerly jet exhibits a distinct eastward displacement and modification of its core, while the SAH configuration also departs progressively from its climatological position. After the onset, the circulation anomaly reaches its most pronounced configuration at Day + 2 (Fig. 4f). Strong negative U200 anomalies dominate eastern China and extend eastward over the western Pacific, while

positive anomalies persist farther upstream over central Asia. The resulting zonal-wind anomaly pattern forms a pronounced upstream–downstream contrast, indicating that the upper-tropospheric circulation perturbation continues to evolve after the drought-to-flood transition rather than being confined to the onset day. The jet core is correspondingly displaced and reorganized, and the SAH exhibits a more pronounced departure.

Figure 5 further reveals the evolution of the mid-tropospheric circulation and IVT anomalies associated with DTFAA events in MRC. From Day − 8, pronounced 500-hPa geopotential height anomalies develop across the Eurasian mid–high latitudes, accompanied by organized anomalies in IVT (Fig. 5a). A positive geopotential height anomaly is evident over central Asia, while negative anomalies extend downstream toward East Asia. This upstream–downstream contrast becomes progressively more organized during the subsequent days, indicating the development and eastward evolution of a large-scale midlatitude circulation disturbance. The evolution is broadly consistent with the upper-tropospheric U200 anomaly pattern in Fig. 4a. From Day − 6 to Day − 4, the positive 500-hPa height anomaly over central Asia strengthens and extends eastward, whereas negative height anomalies become increasingly evident over East Asia. This configuration is accompanied by a gradual reorganization of the moisture-transport field. During the same period, anomalous moisture transport begins to develop over eastern China and adjacent regions, indicating that the atmospheric circulation perturbation is already modifying the regional moisture supply before the onset of the flood phase (Figs. 5b, 5c). The circulation and moisture fields undergo a more pronounced transition between Day − 2 and Day 0. By Day − 2, the positive height anomaly over central and eastern Eurasia becomes more extensive, while negative anomalies become concentrated over East Asia (Fig. 5d). At the same time, significant anomalous IVT vectors increasingly converge toward the MRC, indicating enhanced moisture transport into the region. The 5880-gpm contour indicated the Western Pacific Subtropical High (WPSH) also westerly shifts relative to its climatological position. By Day 0, this adjustment becomes particularly pronounced, with the 5880-gpm contour extending farther westward toward eastern China (Fig. 5e). Concurrently, strong moisture-transport anomalies are directed from the subtropical western Pacific and adjacent low-latitude regions toward the MRC. This configuration favors an enhanced supply of warm, moist air to the region precisely when the upper- and mid-tropospheric circulation is undergoing rapid reorganization. Following the onset, the circulation anomaly remains pronounced at Day + 2. Positive 500-hPa height anomalies dominate much of central and eastern Eurasia. The moisture-transport anomalies also persist over eastern China, indicating that the enhanced moisture supply does not terminate immediately after the drought-to-flood transition (Fig. 5f).

3.3 Dynamic mechanisms underlying DFAA events

The underlying dynamical evolution is further examined through the framework of upper-tropospheric waveguiding and jet interactions, elucidated by the PV_y (Fig. 6). During the phase Day − 8 to Day − 2, PV_y exhibits meridional differentiation (Figs. 6a–d). Influenced by the deceleration of the high-latitude upper-tropospheric westerlies and anticyclonic anomalies (Figs. 4a–d), negative PV_y anomalies are excited in the upper troposphere over high latitudes at Day − 4 (Fig. 6c). The suppression of PV_y

impedes downstream wave energy dispersion and bolsters local nonlinear maintenance, facilitating the establishment and persistent stalling of the Ural–Siberian blocking (Figs. 5a–c). On the other hand, pronounced positive PV_y is maintained across the mid-latitudes (35°N–50°N), forming a robust and coherent Rossby waveguide that guides eastward wave energy propagation across Eurasia. Crucially, the subtropical domain (25°N over the western North Pacific) experiences a reversal in PV_y during this period (Fig. 6c). Crucially, the intense upper-tropospheric anticyclone of SAH anchors the southern flank of this conduit. The sharp PV_y gradient along the northern periphery of the SAH acts as a dynamical rigid southern boundary, effectively preventing wave energy from leaking equatorward and tightly anchoring the mid-latitude wave train within this zonal track. The dynamical trapping induced by localized negative PV_y prevents wave energy from dispersing equatorward while fostering anticyclonic vorticity accumulation, generating a barotropic tropospheric positive geopotential height anomaly (Fig. 6d). This forces the WPSH to abruptly extend westward and shift northward toward coastal southeast China and adjacent oceans (Fig. 5d). Although MRC remains gripped by preceding drought, the synergistic forcing of the intact mid-latitude waveguide and the subtropical anticyclonic negative PV_y enables the downstream mid-latitude cold trough to dig southeastward while allowing moist southwesterlies along the WPSH to begin surging northward. Consequently, baroclinicity progressively develops over MRC.

As the event transitions into the flooding phase, the upper-tropospheric jet and the mid-latitude PV_y waveguide undergo violent dynamical adjustments (Figs. 4e and 6e). Starting from Day − 2, the subtropical jet intensifies sharply and extends eastward over MRC and adjacent oceans (Figs. 4d–f), generating intense meridional horizontal wind shear characterized by northern acceleration and southern deceleration ($\partial U/\partial y < 0$). Driven by the abrupt zonal acceleration of the westerly jet core and dynamical contribution of U_{yy} along its southern flank, upper-level PV_y across mid-latitude East Asia and the western North Pacific surges explosively. Broad positive PV_y anomalies rapidly intensify along the mid-latitude jet axis, demarcating an efficient wave energy corridor (Figs. 6e and 6f). This coherent PV_y conduit confers waveguide dispersion efficiency, directly channeling Rossby wave energy trapped within the upstream Ural blocking downstream (Fig. 5e). Concurrently, ageostrophic wind shear in the jet exit region induces a transverse secondary circulation. The resulting divergent suction over MRC feeds back to deepen the mid-tropospheric cyclonic trough. The steepened pressure gradient between the trough and the westward-extended WPSH triggers an explosion of the low-level jet and deep moisture flux convergence (Figs. 4e and 4f). The moisture which has been accumulating since Day − 8 surges northward, clashing with the southward dry air over MRC. This triggering process terminates the antecedent drought and completes the full outbreak of the DTFAA events.

To confirm the triggering mechanism of downstream wave train dispersion on DTFAA events, we further examined the Hovmöller diagram of PV_y and meridional wind anomalies averaged over 35°N–50°N (Fig. 7). From Day − 8 to Day − 3, positive PV_y anomalies and meridional wind disturbances remained stagnant over Eurasia (60°E–80°E), exhibiting quasi-stationary characteristics that maintained the upstream blocking and locked the large-scale circulation configuration. Starting from Day − 2, concomitant with the intensification of jet, a continuous corridor composed of enhanced PV_y rapidly

expanded eastward. Acting as an efficient wave energy conduit, this waveguide abruptly channeled the wave energy previously trapped upstream toward MRC via prominent group velocity dispersion. By Day 0, an explosive surge of PV_y rapidly penetrated the MRC, accompanied by a sharp intensification of alternating positive and negative meridional wind anomalies. The eastward propagation of this wave packet directly triggered deep tropospheric ascent on the transition onset day, verifying that the enhanced wave train dispersion guided by the jet acts as a switch to trigger the occurrence of the DTFAA events.

3.4 Crop-Specific Spatiotemporal Patterns of DTFAA Exposure

Figure 8 presents the spatial distributions of mean DTFAA frequency and intensity exposure for major crops in China during 2000–2019, revealing pronounced regional heterogeneity across the country's principal agricultural zones. Both frequency and intensity exposure are concentrated in the major grain-producing regions, with high-frequency exposure particularly evident in the Northeast China Plain, North China Plain, and the middle–lower reaches of the Yangtze River. In contrast, exposure generally decreases toward the western and southern margins of the agricultural domain. This broad spatial gradient reflects the combined influence of regional hydrothermal conditions, crop distribution, and the concentration of cultivated land in lowland plains, whereas mountainous and less intensively cultivated regions contribute relatively little to the overall exposure.

Marked differences are also evident among cropping systems. Maize and wheat exhibit relatively extensive and contiguous high-exposure belts (Figs. 8a, 8d, 8e, and 8h), corresponding closely to their large-scale cultivation across the northern agricultural plains. Their widespread exposure suggests that DTFAA represents a substantial climatic constraint for these crops because reproductive development frequently coincides with periods of high temperature and atmospheric water deficit. This finding is consistent with previous global evidence showing that exposure to critical temperatures during the reproductive period can increase substantially even when changes in seasonal mean temperature alone provide a poor indication of crop heat risk (Praba et al., 2009). Rice, especially late rice, displays a more fragmented and spatially heterogeneous exposure pattern (Figs. 8c, 8g). Rather than forming broad continuous belts, high-exposure areas occur as scattered clusters across southern China. This distribution is consistent with the highly fragmented agricultural landscape of southern rice-growing regions, where complex topography, heterogeneous cropping calendars, irrigation conditions, and localized land use generate substantial spatial variation in crop exposure. Differences between single (Figs. 8b, 8f) and late rice further indicate that crop calendars are an important determinant of climatic exposure: even within the same geographic region, differences in reproductive timing can place crops under markedly different thermal environments. Regions with frequent DTFAA events are generally also associated with elevated intensity exposure, especially across the major northeastern and central agricultural plains. This indicates that these regions are not merely experiencing isolated extreme events but are subject to a recurrent and potentially cumulative climate hazard. Nevertheless, the spatial extent of the highest-intensity exposure is considerably more restricted than that of high-frequency exposure.

Figure 9 illustrates the spatial and temporal variations in maize, single and early rice (SR&ER), late rice (LR), and wheat exposure to DTFAA events across the MRC during 2000–2019. Both the frequency and intensity of exposure exhibit pronounced crop-specific and regional differences (Figs. 9a–h). Maize shows widespread positive trends in both frequency and intensity exposure, particularly across North China, Northeast China, and parts of Southwest China, with significant increases occurring over a substantial fraction of its cultivated area. SR&ER also exhibits positive trends in both metrics across the middle and lower reaches of the Yangtze River Basin and northeastern China, although these increases are predominantly nonsignificant. In southwestern China, SR&ER shows slight decreases in frequency exposure but generally positive trends in intensity exposure. By contrast, LR exhibits relatively weak and spatially heterogeneous trends, with no clear overall tendency in either frequency or intensity exposure. Wheat shows predominantly positive trends in both metrics, particularly across the Huang-Huai-Hai Plain, whereas scattered negative trends occur mainly along the northern margins of its cultivated area and are mostly nonsignificant. Overall, maize has the largest proportion of grid cells exhibiting significant increases, while SR&ER is characterized by predominantly positive but mostly nonsignificant trends. Wheat and LR show more spatially heterogeneous patterns, with both positive and negative trends distributed across their respective cultivated areas.

The temporal variations further highlight these crop-specific differences (Figs. 9i–l). Maize exhibits significant upward trends in both frequency and intensity exposure during 2000–2019, with frequency increasing at approximately 0.12 per year and intensity increasing at approximately 0.10 per year ($p < 0.05$). Wheat also shows positive trends in both metrics, although neither trend is statistically significant. SR&ER exhibits a weak increasing tendency in frequency exposure, whereas its intensity exposure remains relatively stable throughout the study period. Consistent with the spatial patterns, LR shows little overall temporal trend in either metric. The magnitude of interannual variability also differs among crops, with maize and wheat generally exhibiting larger fluctuations than the two rice types. This contrast may be related, at least in part, to differences in hydroclimatic conditions and water availability between the predominantly rain-fed cropping systems in northern China and the more humid and irrigated rice-growing regions in southern China. Collectively, these results indicate a pronounced increase in DTFAA exposure for maize, particularly in northern China, whereas exposure for rice crops has remained comparatively stable or increased only modestly. The contrasting spatial and temporal responses among crops underscore the importance of crop-specific strategies for managing increasing exposure to hydrological extremes.

4. Conclusions and discussion

DTFAA represents a distinctive compound hydroclimatic hazard because the rapid succession from dry to wet conditions can generate impacts that are not adequately captured by treating drought and flood as independent hazards. Here, we extend a daily SWAP-based framework to the MRC during the principal flood season (May-September). Using observations from 1,903 meteorological stations during 1961–2023, we identify 3,575 DTFAA events and find that most transitions occur within 1–2 days. This result provides direct observational evidence that DTFAA evolves substantially faster than can be resolved by

conventional monthly indices (Wu et al., 2006; Yang et al., 2022). The spatial distribution, characterized by relatively frequent events in the middle and lower Yangtze River Basin, southeastern China, and parts of North China, is also consistent with previous evidence identifying eastern and southern China as major hotspots of drought–flood alternation. However, event frequency and intensity exhibit distinct spatial patterns: regions with frequent transitions do not necessarily experience the most intense events. Long-term trends provide further evidence of increasing DTFAA risk across the MRC. The regional mean frequency increases by approximately 0.29 events decade^{-1}, while intensity increases by 0.26 decade^{-1}; both trends are statistically significant ($p < 0.05$). Positive trends are particularly evident in the eastern and southern portions of the region, although statistically significant trends remain spatially limited. These findings complement previous studies reporting increases in DTFAA occurrence in China and globally (Bai et al., 2023; Barendrecht et al., 2024). Importantly, our results indicate that the regional increase in DTFAA risk is expressed more strongly through increasing event frequency than through a pervasive intensification of individual events. Thus, increasing exposure may result primarily from more frequent transitions between hydroclimatic states rather than from a uniform increase in the magnitude of individual events.

Composite analysis provides further insight into the temporal evolution of the large-scale circulation governing DTFAA events. Several days before onset, a positive geopotential-height anomaly develops over central Eurasia, while negative anomalies emerge downstream over East Asia. The circulation then undergoes rapid reorganization, accompanied by the westward extension of the WPSH and enhanced moisture transport toward the MRC. This evolution indicates that the drought to flood transition is not simply a local reversal in precipitation but rather the culmination of a progressively organized large-scale circulation disturbance. During the precursor stage, high-latitude negative PV_y associated with Ural-Siberian blocking suppresses downstream wave dispersion, trapping wave energy upstream. Simultaneously, a coherent mid-latitude Rossby waveguide corridor develops farther south, rigidly anchored on its southern flank by the sharp PV_y gradient along the northern periphery of the SAH, which prevents equatorward energy leakage. Beginning approximately two days before onset, rapid strengthening, eastward extension, and intense horizontal wind shear of the upper-tropospheric subtropical jet abruptly open a waveguide conduit. This channel acts as a dynamical conduit, abruptly releasing the upstream-trapped wave energy via rapid downstream group velocity dispersion toward MRC. Near onset, jet exit-region dynamics induce powerful upper-level divergent suction, which deepens the mid-tropospheric trough, steepens the pressure gradient against the WPSH, and triggers an explosion of low-level jet moisture convergence. The violent clash between dry northerlies and surging warm, moist southwesterlies drives extreme precipitation, terminating the drought. This circulation evolution complements the recently proposed multiscale interpretation of DTFAA events over the Yangtze River Basin (Zhao et al., 2026). The rapidity of this evolution further highlights the importance of temporal scale in understanding DTFAA events. Previous work has emphasized that drought to flood alternation can involve multiple temporal and spatial scales, with the relevant processes spanning from sub-seasonal variability to synoptic-scale events (Wang et al., 2024; Tu et al., 2022). Our results reveal that the transition itself is concentrated within only a few days, while the associated heavy precipitation

may develop over hours or even shorter periods. Consequently, the mechanisms responsible for rapid drought-to-flood transitions cannot be adequately characterized using coarse temporal resolutions. Resolving the synoptic-scale circulation evolution and its interaction with moisture transport is therefore essential for understanding how a preexisting dry state can transition abruptly into a flood-producing state.

The agricultural exposure results extend previous DTFAA research by linking atmospheric hazard characteristics to crop-specific spatial patterns. High exposure is concentrated across major agricultural plains, particularly the Northeast China Plain, North China Plain, and middle and lower Yangtze River regions. Maize and wheat exhibit broad, contiguous exposure belts, whereas rice exposure is more fragmented. These differences reflect the combined effects of crop distribution, local hydroclimate, irrigation, topography, and phenological timing (Meza et al., 2020; Murthy et al., 2015; Praba et al., 2009). The pronounced increase in maize exposure is noteworthy because it demonstrates that changes in DTFAA hazard can translate unevenly across agricultural systems. The ChinaCropPhen1km dataset provides a spatially explicit basis for resolving differences in crop calendars and associated exposure (Luo et al., 2020). Thus, these results extend beyond hazard climatology toward an impact-oriented assessment, showing that the same atmospheric event can produce different levels of agricultural exposure depending on crop type and phenological stage.

Several limitations should nevertheless be acknowledged. First, DTFAA identification is based on precipitation and therefore does not directly capture responses in soil moisture, evapotranspiration, runoff, or groundwater. Although sensitivity tests support the 8-day transition criterion, alternative definitions may identify somewhat different event populations. Second, the agricultural analysis characterizes potential exposure rather than realized crop damage and does not explicitly account for irrigation, management practices, cultivar differences, yield sensitivity, or adaptive responses. Future studies should integrate land-surface observations, hydrological variables, crop-yield records, and event-based attribution methods to better quantify these processes and distinguish hazard exposure from realized agricultural impacts.

Declarations

Declarations

The authors have no relevant financial or non-financial interests to disclose.

Funding

This research was funded by the Furong Program for Young Talents in Science and Technology Innovation (Grant No. 2026RC3264) and the Open Research Fund Project of Jiangsu Province Key Laboratory for Risk Warning of Severe Convective Disasters (Grant No. QDL2026M06).

Author Contributions

JL contributed to this work's conception. JL, YS, QM and DW provided the main idea, developed the methodology, and prepared the validation. YS, AX, QM and CZ wrote the manuscript and prepared figures. SS, TJ, CZ and QM reviewed and edited the manuscript. All authors read and approved the final manuscript.

Data Availability

The station-based daily precipitation dataset was provided by the National Meteorological Information Center of the China Meteorological Administration and is available at https://data.cma.cn/en after registration and signing an agreement with the data-sharing policy. ERA5 reanalysis datasets were obtained from ECMWF through the Copernicus Climate Data Store (https://cds.climate.copernicus.eu/datasets/reanalysis-era5-pressure-levels?tab=overview and https://cds.climate.copernicus.eu/datasets/reanalysis-era5-single-levels?tab=overview). The crop phenology dataset was obtained from the National Ecosystem Science Data Center and is available at (https://www.nesdc.org.cn/sdo/detail?id=627dfc4b7e28172589c2deaa).

References

1. Bai X, Zhao C, Tang Y, Zhang Z, Yang B, Wang Z (2023) Identification, physical mechanisms and impacts of drought–flood abrupt alternation: a review. Front Earth Sci 11:1203603. https://doi.org/10.3389/feart.2023.1203603
2. Barendrecht MH, Matanó A, Mendoza H et al (2024) Exploring drought-to-flood interactions and dynamics: A global case review. WIREs Water 11(4):e1726. https://doi.org/10.1002/wat2.1726
3. Bi W, Li M, Weng B et al (2023) Drought-flood abrupt alteration events over China. Sci Total Environ 875:162529. https://doi.org/10.1016/j.scitotenv.2023.162529
4. Chen T, Chen Y, Fang C et al (2024) Fine characteristics of the July 2023 extreme rainfall in North China and associated synoptic weather patterns. Acta Meteorol Sin 82(5):600–614. https://doi.org/10.11676/qxxb2024.20240036
5. Chen Z, Li X, Zhang X et al (2025) Global drought-flood abrupt alternation: Spatio-temporal patterns, drivers, and projections. Innov Geosci 100113. https://doi.org/10.59717/j.xinn-geo.2024.100113
6. Dai S, Zhang Q, Wang J et al (2026) Drought-flood abrupt alternation in the Haihe Plain: Synoptic circulation patterns and yield impacts on summer maize. Agric Water Manage 334:110706. https://doi.org/10.1016/j.agwat.2026.110706
7. De Vries AJ, Armon M, Klingmüller K, Portmann R, Röthlisberger M, Domeisen DIV (2024) Breaking Rossby waves drive extreme precipitation in the world's arid regions. Commun Earth Environ 5(1):493. https://doi.org/10.1038/s43247-024-01633-y

8. Gimeno L, Nieto R, Eiras-Barca J et al (2026) Tracing atmospheric heat and moisture pathways to understand compound drought–heatwave events. Weather Clim Extremes 53:100923. https://doi.org/10.1016/j.wace.2026.100923
9. Götte J, Brunner MI (2024) Hydrological drought-to-flood transitions across different hydroclimates in the United States. Water Resour Res 60(7). https://doi.org/10.1029/2023WR036504. e2023WR036504
10. Gu J, Zheng Y, Guo J et al (2026) Analysis of meteorological to hydrological propagation characteristics of drought-to-flood abrupt alternation events in near-natural catchments. J Hydrol Reg Stud 67:103875. https://doi.org/10.1016/j.ejrh.2026.103875
11. He J, Yang X-H, Li J-Q, Jin J-L, Wei Y-M, Chen X-J (2015) Spatiotemporal variation of meteorological droughts based on the daily comprehensive drought index in the Haihe River basin, China. Nat Hazards 75(2):199–217. https://doi.org/10.1007/s11069-014-1158-8
12. He N, Yin J, Liu P, Fu X, Zhang Q, Cheng L, Moulds S, Volchak A (2025) Global increases in dry-wet abrupt alternation events under climate change. Geophys Res Lett 52(18): e2025GL117322. https://doi.org/10.1029/2025GL117322
13. Henny L, Kim K-M (2025) The changing nature of atmospheric rivers. J Clim 38(6):1435–1456. https://doi.org/10.1175/JCLI-D-24-0234.1
14. Hersbach H, Bell B, Berrisford P et al (2020) The ERA5 global reanalysis [Dataset]. Q J R Meteorol Soc 146(730):1999–2049. https://doi.org/10.1002/qj.3803
15. Hu G, Xu K, Ge F, Huang Q-L, Leung JC-H, Jin Z, Wang P (2025) Diversity of the Drought-Flood abrupt Alternation: Dynamic Processes during the Preflood season over South China. J Clim 38(21):6227–6243. https://doi.org/10.1175/JCLI-D-24-0742.1
16. Ji C, Agathokleous E, Ju L et al (2025) Growing threat of climate-induced abrupt dry-wet transitions in Northern China. Atmos Res 326:108325. https://doi.org/10.1016/j.atmosres.2025.108325
17. Kumar A, Arya DS (2025) Spatiotemporal analysis and mechanisms of drought flood abrupt alternation events in India. J Hydrol Reg Stud 62:102992. https://doi.org/10.1016/j.ejrh.2025.102992
18. Li J, Wang S, Zhu J et al (2025) Accelerated shifts from heatwaves to heavy rainfall in a changing climate. npj Clim Atmos Sci 8(1):214. https://doi.org/10.1038/s41612-025-01113-w
19. Li X, Li S, Wang L et al (2026) Spatiotemporal variability of drought-flood abrupt alternation events in Southwest China during 1961 to 2024. Theor Appl Climatol 157(2):96. https://doi.org/10.1007/s00704-026-06024-1
20. Liu Y, Yao S, Yan M et al (2026) Interdecadal mechanistic shift of summer rapid flood-drought transition over the middle-lower reaches of the Yangtze River: From the East Asia-Pacific teleconnection to the western Pacific subtropical high. Int J Climatol 46(6):e70321. https://doi.org/10.1002/joc.70321
21. Lu E (2009) Determining the start, duration, and strength of flood and drought with daily precipitation: Rationale. Geophys Res Lett 36(12). https://doi.org/10.1029/2009GL038817

22. Luo D, Zhang W, Zhong L, Dai A (2019) A Nonlinear Theory of Atmospheric Blocking: A Potential Vorticity Gradient View. J Atmos Sci 76:2399–2427. https://doi.org/10.1175/JAS-D-18-0324.1
23. Luo Y, Zhang Z, Chen Y, Li Z, Tao F (2020) ChinaCropPhen1km: A high-resolution crop phenological dataset for three staple crops in China during 2000–2015 based on leaf area index (LAI) products. Earth Syst Sci Data 12(1):197–214. https://doi.org/10.5194/essd-12-197-2020
24. Matanó A, de Ruiter MC, Koehler J et al (2022) Caught between extremes: Understanding human-water interactions during drought-to-flood events in the Horn of Africa. Earths Future 10(9). https://doi.org/10.1029/2022EF002747. e2022EF002747
25. Meza I, Siebert S, Döll P et al (2020) Global-scale drought risk assessment for agricultural systems. Nat Hazards Earth Syst Sci 20(2):695–712. https://doi.org/10.5194/nhess-20-695-2020
26. Murthy CS, Laxman B, Sai MVRS (2015) Geospatial analysis of agricultural drought vulnerability using a composite index based on exposure, sensitivity and adaptive capacity. Int J Disaster Risk Reduct 12:163–171. https://doi.org/10.1016/j.ijdrr.2015.01.004
27. Na W, Najafi MR (2024) Rising risks of hydroclimatic swings: a large ensemble study of dry and wet spell transitions in North America. Global Planet Change 238:104476. https://doi.org/10.1016/j.gloplacha.2024.104476
28. Praba ML, Cairns JE, Babu RC et al (2009) Identification of physiological traits underlying cultivar differences in drought tolerance in rice and wheat. J Agron Crop Sci 195(1):30–46. https://doi.org/10.1111/j.1439-037X.2008.00341.x
29. Roderick TP, Wasko C, Sharma A (2019) Atmospheric moisture measurements explain increases in tropical rainfall extremes. Geophys Res Lett 46(3):1375–1382. https://doi.org/10.1029/2018GL080833
30. Seneviratne SI, Zhang X, Adnan M et al (2021) Weather and climate extreme events in a changing climate. Climate change 2021: The physical science basis: Working group I contribution to the sixth assessment report of the intergovernmental panel on climate change: 1513–1766. https://doi.org/10.1017/9781009157896.013
31. Shan L, Zhang L, Song J, Zhang Y, She D, Xia J (2018) Characteristics of dry-wet abrupt alternation events in the middle and lower reaches of the Yangtze River Basin and the relationship with ENSO. J Geogr Sci 28(8):1039–1058. https://doi.org/10.1007/s11442-018-1540-7
32. Shi W, Huang S, Liu D, Huang Q, Han Z, Leng G, Wang H, Liang H, Li P, Wei X (2021) Drought-flood abrupt alternation dynamics and their potential driving forces in a changing environment. J Hydrol 597:126179. https://doi.org/10.1016/j.jhydrol.2021.126179
33. Shi X, Yang Y, Yuan Z, Ding H, Zhang Y, Chen J, Shi M (2024) Integrating SWAP and SIF anomaly to assess the responses of vegetation to the drought-flood abrupt alternation in the middle and lower reaches of the Yangtze River basin, China. J Hydrol Reg Stud 52:101726. https://doi.org/10.1016/j.ejrh.2024.101726
34. Song Y, Chen H, Wang L, Huang A, Gu W (2026) The memories of soil moisture and soil temperature anomalies in subsequent soil moisture and soil temperature in China. J Geophys Res Atmos 131(2):

e2025JD044117. https://doi.org/10.1029/2025JD044117

35. Swain DL, Prein AF, Abatzoglou JT et al (2025) Hydroclimate volatility on a warming Earth. Nat Rev Earth Environ 6(1):35–50. https://doi.org/10.1038/s43017-024-00624-z
36. Tu X, Pang W, Chen X et al (2022) Limitations and improvement of the traditional assessment index for drought-wetness abrupt alternation. Adv Water Sci 33(4):592–601. https://doi.org/10.14042/j.cnki.32.1309.2022.04.007 in Chinese
37. Wang C, Li K, Santisirisomboon J (2021) Wave activities characteristics during a sudden sharp drought–flood turn event in 2011 in East China. Int J Climatol 41(6):3469–3480. https://doi.org/10.1002/joc.7030
38. Wang H, Wang S, Shu X, He Y, Huang J (2024) Increasing Occurrence of Sudden Turns From Drought to Flood Over China. J Geophys Res Atmos 129(3). https://doi.org/10.1029/2023JD039974. e2023JD039974
39. Wang L, Li Y, Ahmad AS, Ishchanov J et al (2026) Spatiotemporal patterns and teleconnection drivers of drought–flood abrupt alternation in China. Global Planet Change 266:105683. https://doi.org/10.1016/j.gloplacha.2026.105683
40. Wang R, Li X, Zhang Q, Cheng J, Li J, Zhang D, Liu Y (2023) Projection of drought-flood abrupt alternation in a humid subtropical region under changing climate. J Hydrol 624:129875. https://doi.org/10.1016/j.jhydrol.2023.129875
41. Wasko C (2022) Floods differ in a warmer future. Nat Clim Change 12(2):1090–1091. https://doi.org/10.1038/s41558-022-01541-z
42. Wu B, Yan Z, Yan D et al (2026) Linear time-lag effects and nonlinear interactions of global drought-flood abrupt alternation in responses to multiple factors. J Hydrol 670:135161. https://doi.org/10.1016/j.jhydrol.2026.135161
43. Wu Z, Li J, He J et al (2006) Large-scale atmospheric singularities and summer longcycle droughts-floods abrupt alternation in the middle and lower reaches of the Yangtze River. Chin Sci Bull 51(16):2027–2034. https://doi.org/10.1007/s11434-006-2060-x
44. Yang P, Zhang S, Xia J et al (2022) Analysis of drought and flood alternation and its driving factors in the Yangtze River basin under climate change. Atmos Res 270:106087. https://doi.org/10.1016/j.atmosres.2022.106087
45. Yang S, Wu B, Zhang R, Zhou S (2013) Relationship between an abrupt drought-flood transition over mid-low reaches of the Yangtze River in 2011 and the intraseasonal oscillation over mid-high latitudes of East Asia. Acta Meteorol Sin 27(2):129–143. https://doi.org/10.1007/s13351-013-0201-0
46. Yin J, Guo S, Wang J, Chen J, Zhang Q, Gu L, Yang Y, Tian J, Xiong L, Zhang Y (2023) Thermodynamic driving mechanisms for the formation of global precipitation extremes and ecohydrological effects. Sci China Earth Sci 66(1):92–110. https://doi.org/10.1007/s11430-022-9987-0
47. Zhai P, Zhang X, Wan H, Pan X (2005) Trends in Total Precipitation and Frequency of Daily Precipitation Extremes over China. J Clim 18(7):1096–1108. https://doi.org/10.1175/JCLI-3318.1

48. Zhang Y, An X, Sun S, Ma Q, Yan P, Zhou B (2025) Characteristics of boreal summer compound hot-drought events in the Yangtze River Valley and relationships with Indian Ocean Sea surface temperature [Dataset]. Clim Dyn 63(5):226. https://doi.org/10.1007/s00382-025-07709-5
49. Zhao C, Sun Y, Ma Q et al (2026) Multiscale dynamic mechanisms of drought-flood abrupt alternation events in the Yangtze River Basin. J Geophys Res Atmos 131(13). https://doi.org/10.1029/2025JD046199. e2025JD046199
50. Zhou Y, Jia W, Zhang W, Wang H (2026) Mechanisms of ENSO's cross-seasonal modulation of winter–spring atmospheric river activity over East Asia. Atmos Ocean Sci Lett 19(1):100659. https://doi.org/10.1016/j.aosl.2025.100659
51. Zhu Z, Xie K, Jin J, Yu C, Ning Z, Wang Y, Liu Y, Wang G, Zhang J (2026) Spatiotemporal evolution and meteorological–hydrological coupling of drought–flood abrupt alternation events in the Yangtze River Basin during 1980–2024. Adv Clim Change Res. https://doi.org/10.1016/j.accre.2026.08.006

Figures

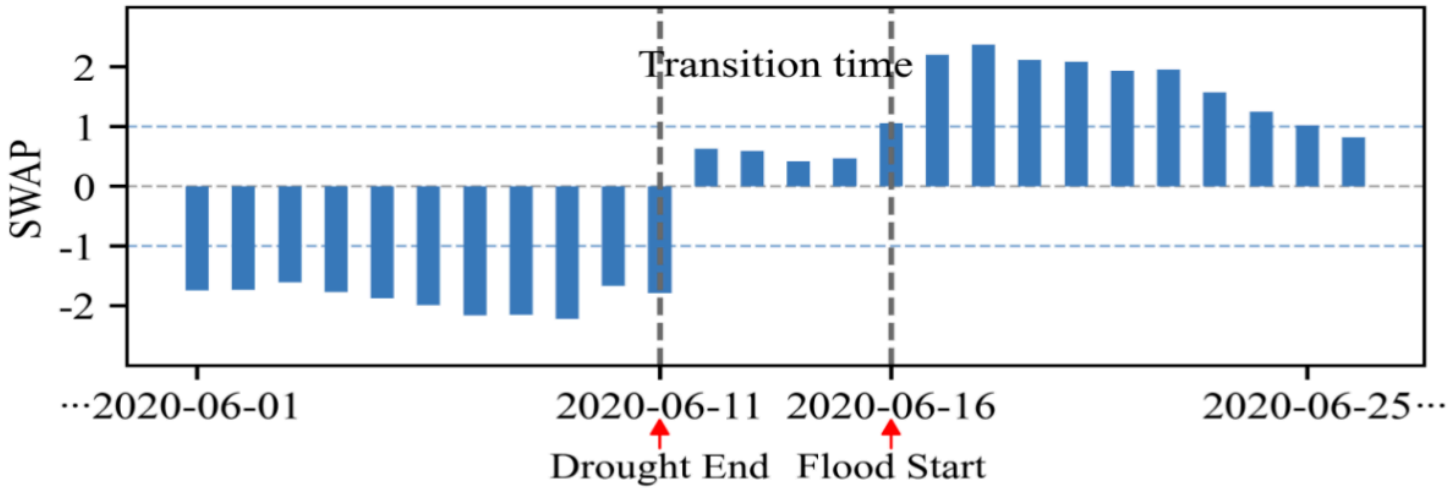


Figure 1

Schematic of the development process of a DTFAA event at Lingbi Station in Anhui province.

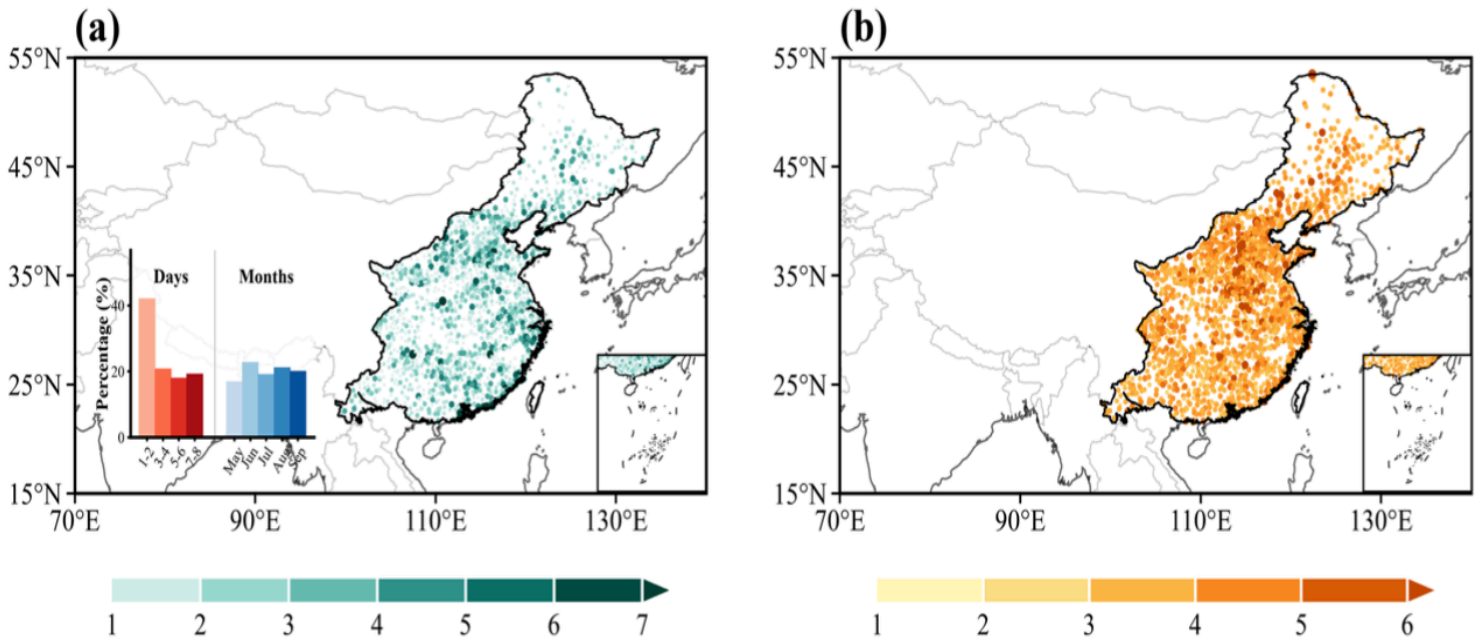


Figure 2

Characteristics of DTFAA events in the MRC from 1961 to 2023: (a) mean frequency (unite: times) and (b) mean intensity. Insets in (a) show the distributions of stations according to transition duration (red bars) and month of occurrence (blue bars).

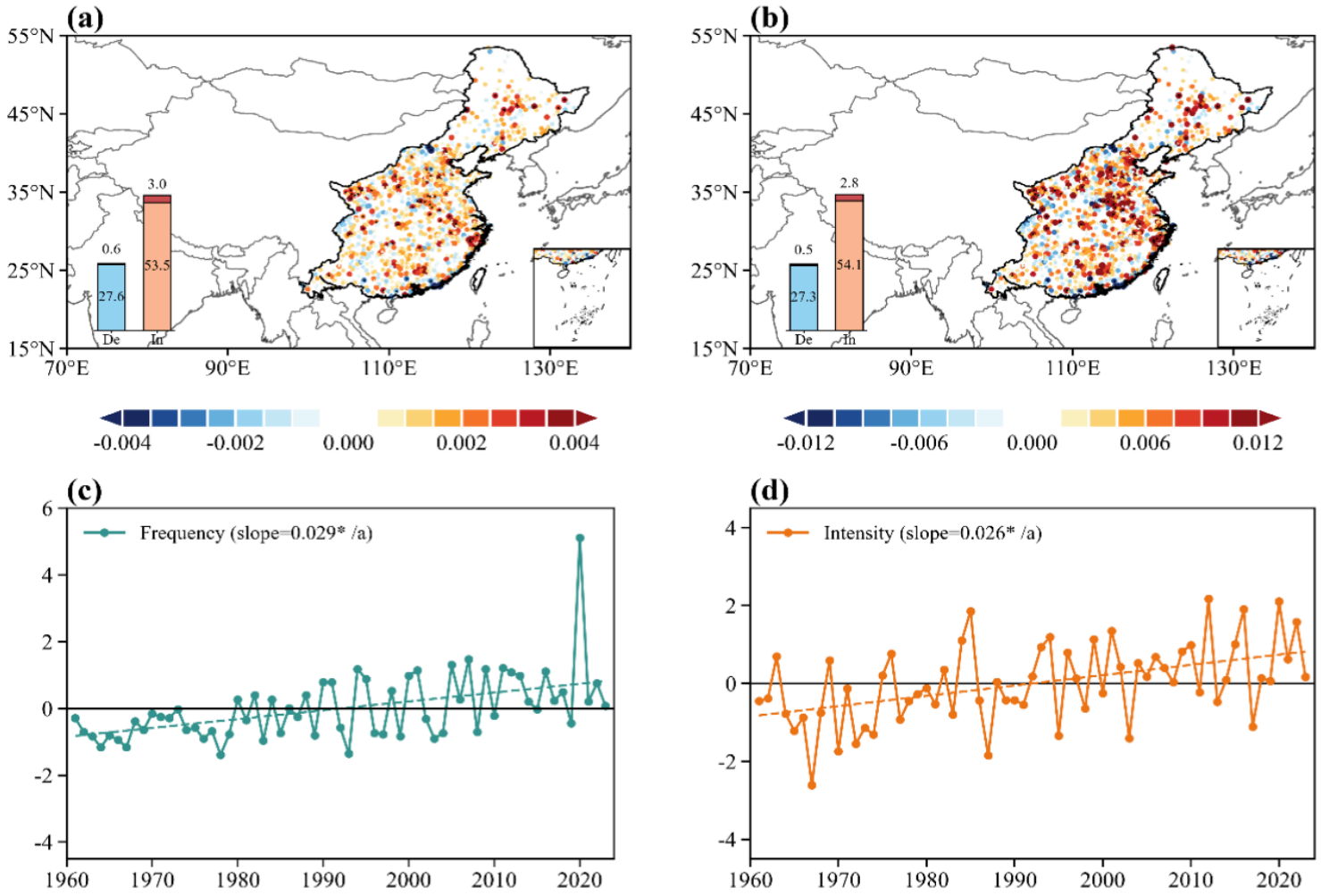


Figure 3

Spatiotemporal characteristics of DTFAA events in the MRC from 1961 to 2023. Linear trends in (a) frequency and (b) intensity. Stippling indicates trends that are statistically significant according to the Student's *t*-test at the 95% confidence level. The bottom-left insets show histograms of the proportions of stations exhibiting increasing or decreasing trends, with stations passing the significance test indicated by dark shading. Time series of (c) frequency and (d) intensity. The dotted line represents the linear trend, and the asterisk (*) denotes a statistically significant trend according to the Student's *t*-test at the 95% confidence level.

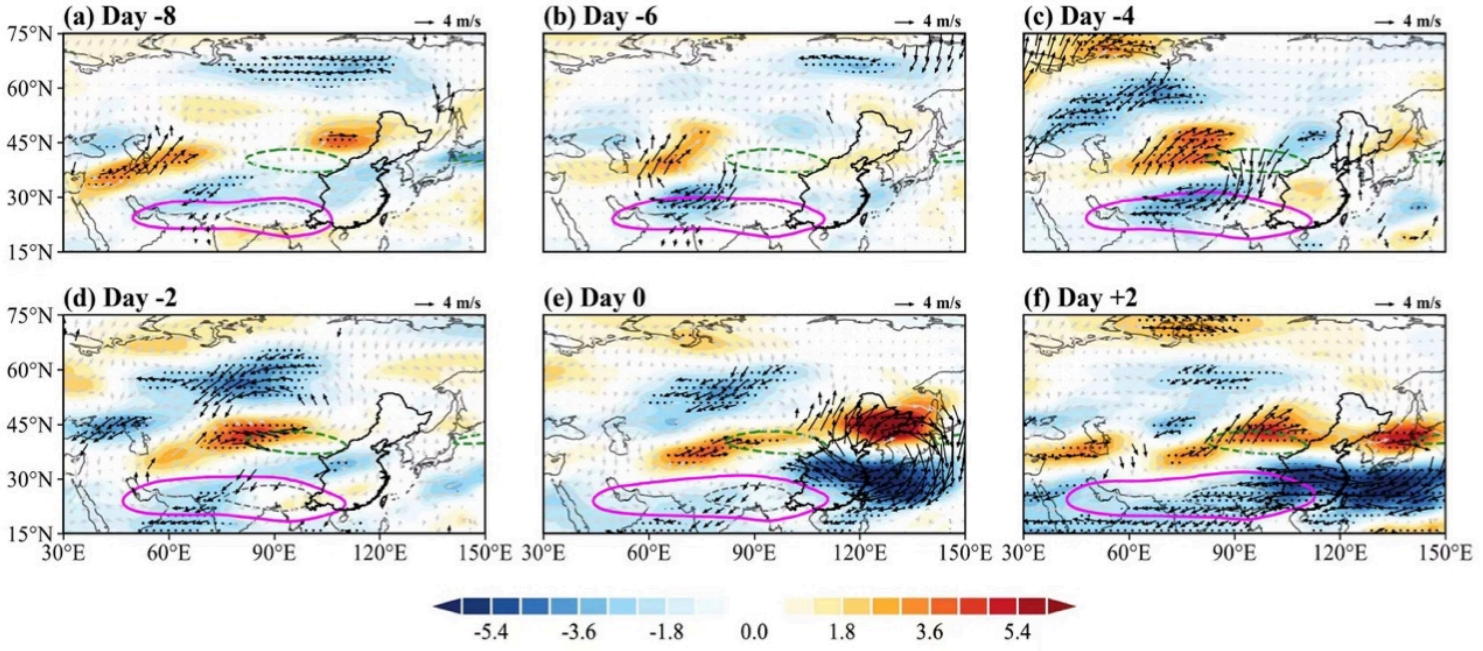


Figure 4

Composite evolution of circulation anomalies at 200-hPa associated with DTFAA events in the MRC from Day -8 to Day +2. Shading denotes composite zonal wind anomalies (U200, m/s), with stippling indicating anomalies significant at the 95% confidence level according to two-tailed Student's *t*-test. Vectors represent composite horizontal winds anomalies (m/s) significant at the 95% confidence level. Solid pink contours indicate the 12,500-gpm geopotential height contour during the composite events, whereas dashed gray contours denote the corresponding climatological contour. Dashed green contours delineate the composite core of the 200-hPa westerly jet, defined by U200 >30 m/s.

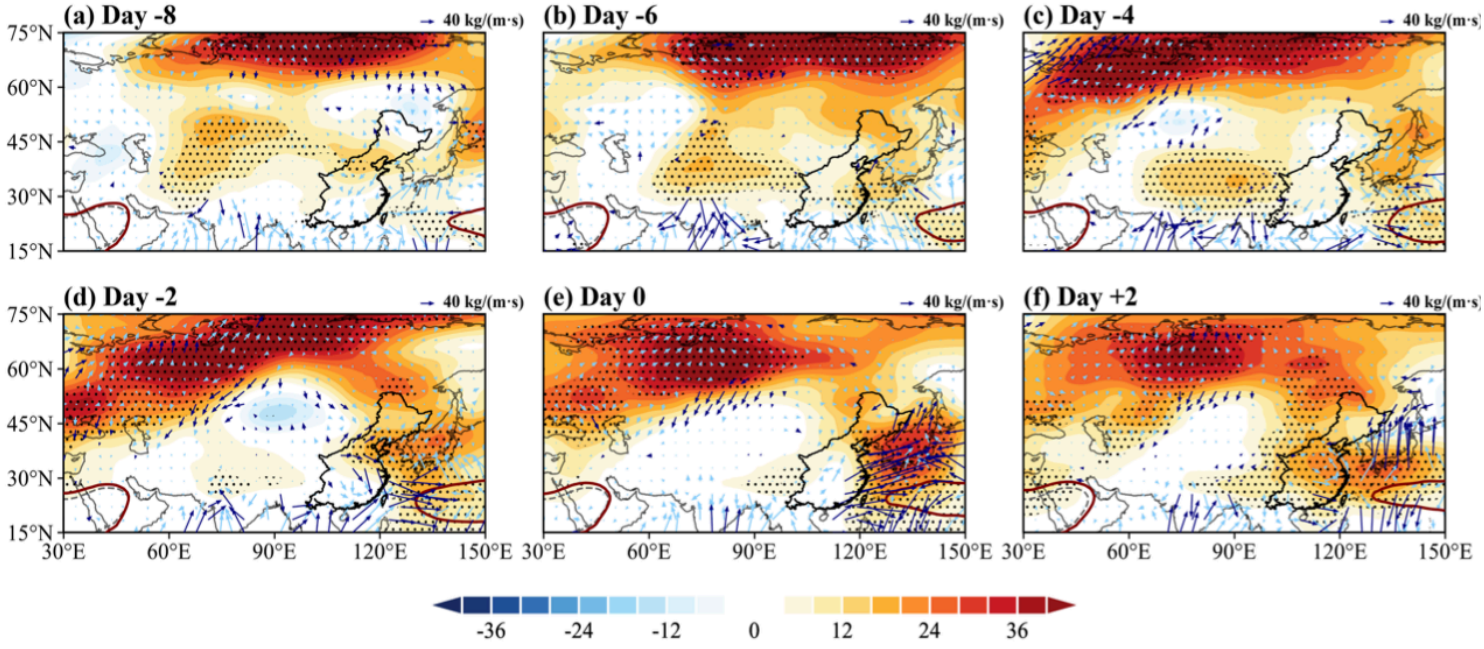


Figure 5

Composite evolution of geopotential anomalies at 500-hPa (shading, gpm) and vertically IVT anomalies (vectors, kg/ (m s)) associated with DTFAA events in the MRC from Day -8 to Day +2. Stippling and deep blue vectors indicate anomalies significant at the 95% confidence level according to two-tailed Student's *t*-test. Solid brown contours indicate the 5880-gpm geopotential height contour during the composite events, whereas dashed gray contours denote the corresponding climatological contour.

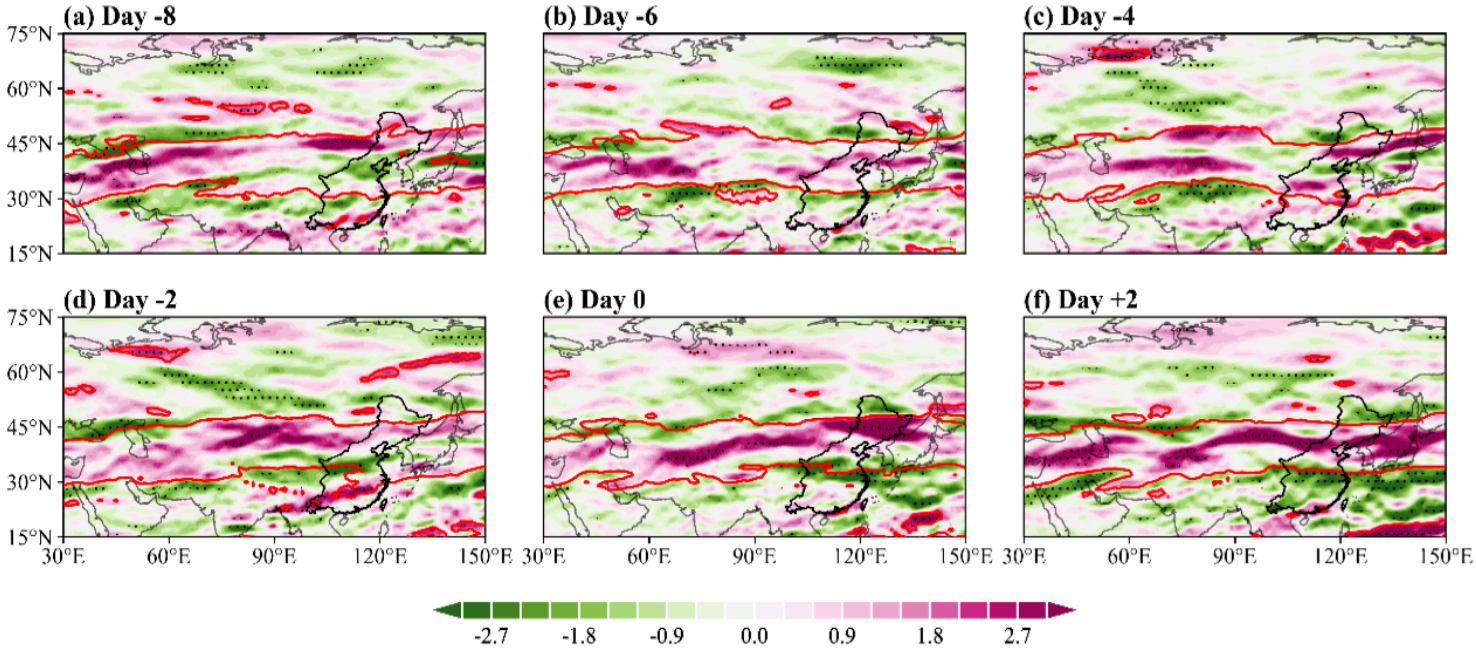


Figure 6

Composite evolution of ⟦"PV" ⟧_y anomalies at 200-hPa (shading) associated with DTFAA events in the MRC from Day -8 to Day +2. Stippling indicating anomalies statistically significant at the 95% confidence level based on a two-tailed t-test. The solid red contours indicate the value of 3, outlining the primary Rossby waveguide corridor.

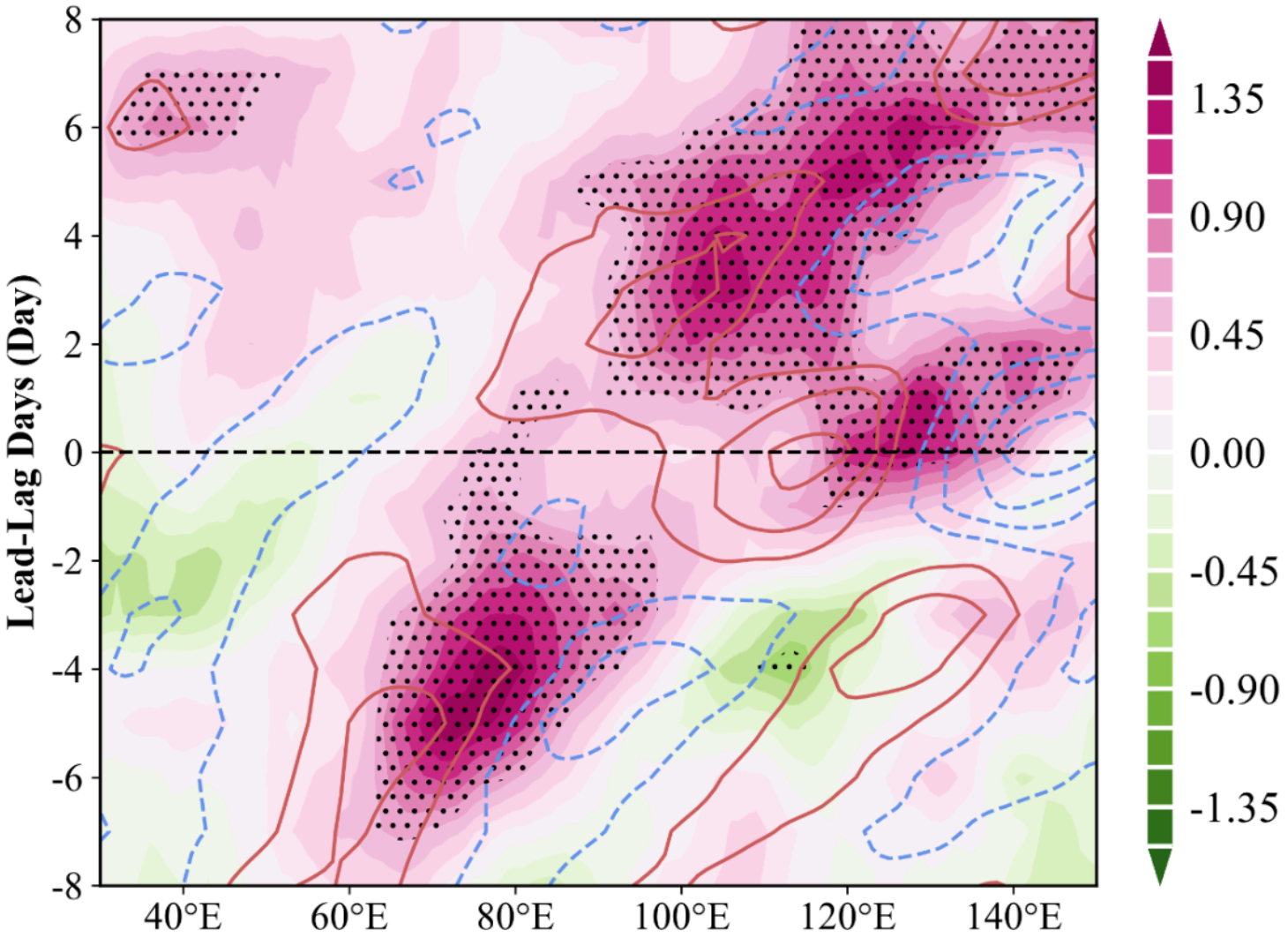


Figure 7

Composite Hovmöller diagrams of ⟦"PV" ⟧_y (shading) and meridional wind anomalies (contours, m/s) at 200-hPa associated with DTFAA events in the MRC from Day -8 to Day +2. Stippling indicating anomalies statistically significant at the 95% confidence level based on a two-tailed t-test. Solid (dashed) contours represent anomalous southerly (northerly) winds (contour interval: 1.5 m/s).

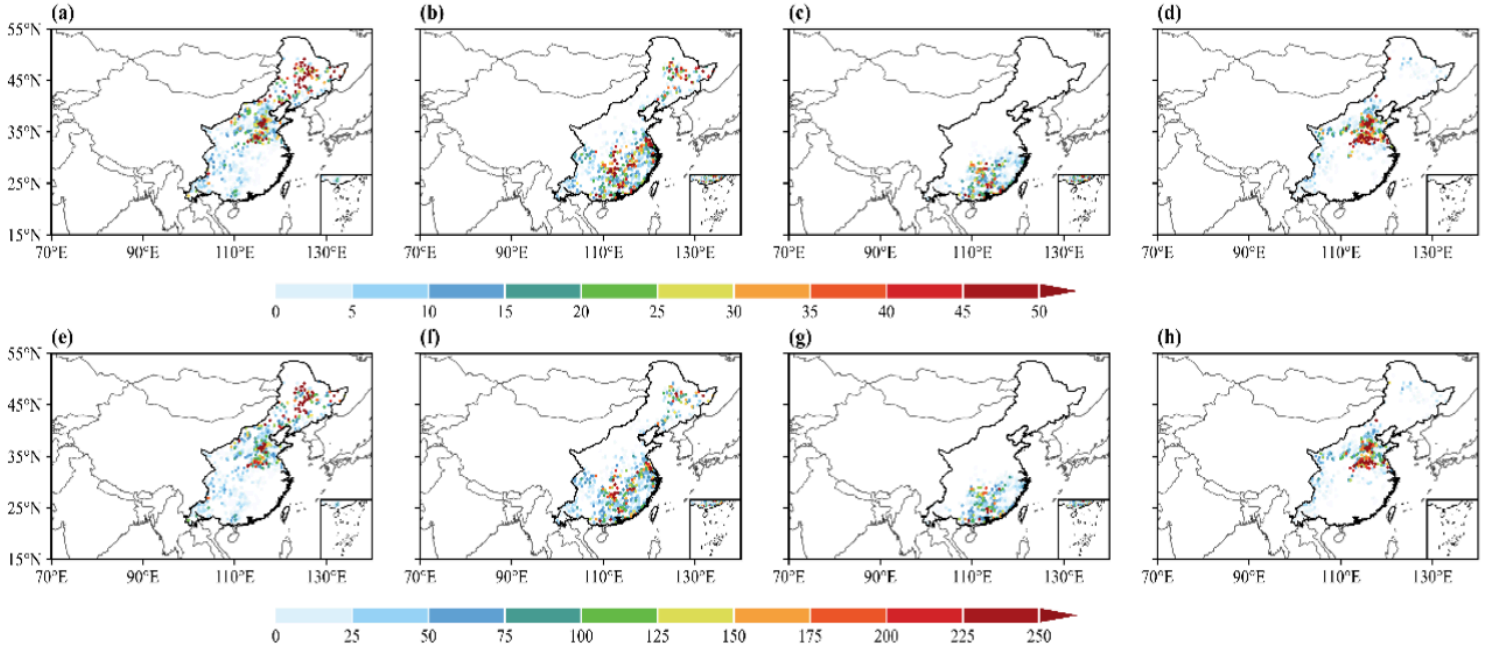


Figure 8

Spatial distributions of mean DTFAA frequency and intensity exposure during 2000–2019. Panels (a–d) show mean DTFAA frequency exposure (times km²), and panels (e–h) show mean DTFAA intensity exposure (km²). From left to right, the columns show maize, single and early rice, late rice, and wheat.

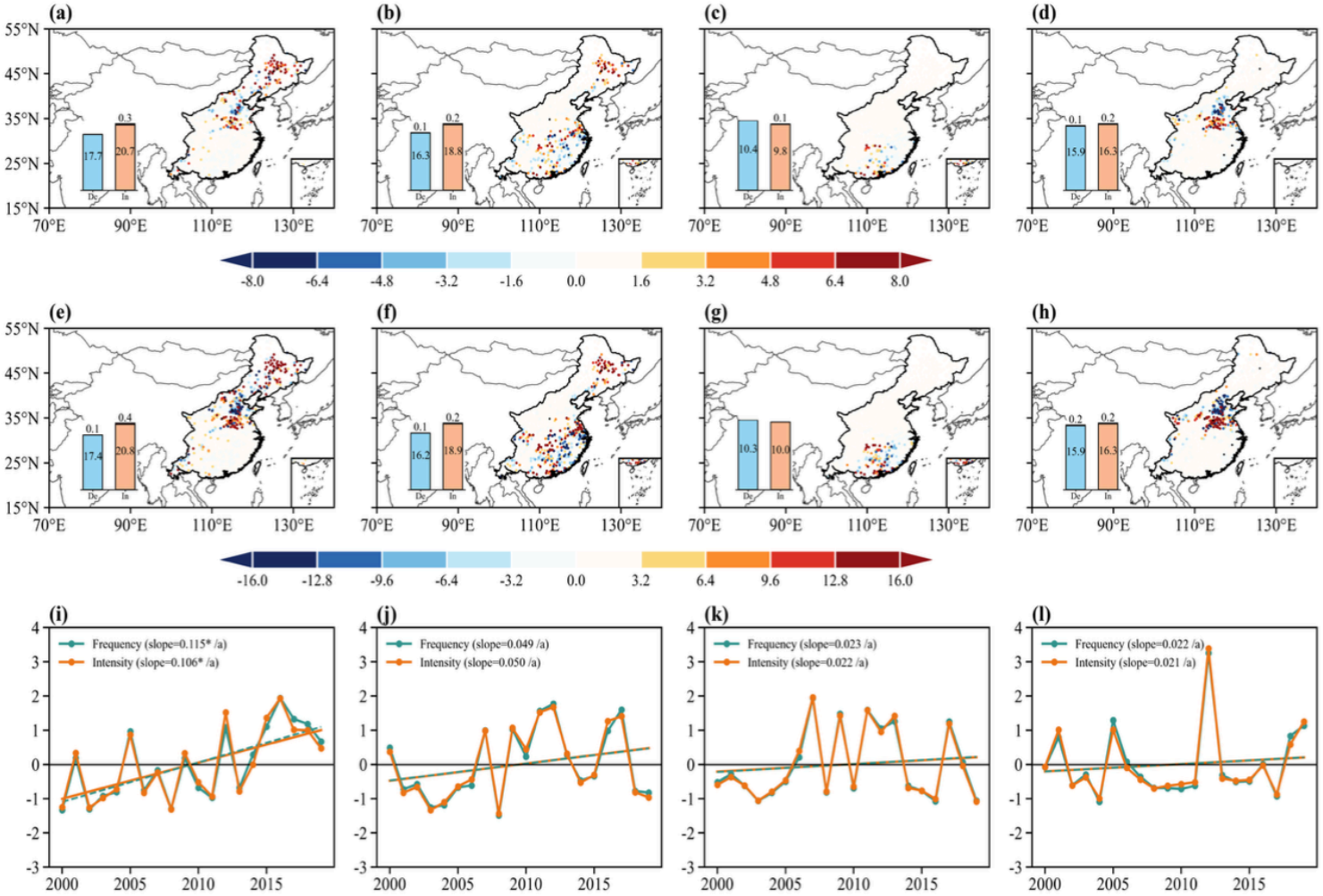


Figure 9

Spatial distributions of trends and temporal variations in DTFAA exposure during 2000–2019. Columns from left to right show maize, single and SR&ER, LR, and wheat. Panels (a–d) show spatial trends in DTFAA frequency exposure (times·km²·yr⁻¹), and (e–h) intensity exposure (km²·yr⁻¹). The inset stacked bar charts indicate the proportions of crop grid cells with significant increases (dark red), nonsignificant increases (light red), significant decreases (dark blue), and nonsignificant decreases (light blue), with significance defined at the 95% confidence level. Panels (i–l) show annual variations in standardized DTFAA frequency and intensity exposure. Orange lines represent frequency exposure, and brown bars represent intensity exposure. Dashed lines indicate the corresponding linear trends, with slopes reported in the legends and asterisks denoting trends significant at the 95% confidence level.

Supplementary Files

This is a list of supplementary files associated with this preprint. Click to download.

- SupportingInformation.docx